Lu, H., Xiao, Y., Liu, Z., Yuan, Y., & Zhou, P. (2024). Interactions of row blades of a marine compressor based on POD analysis. *International Journal of Engine Research*. Advance online publication.
https://doi.org/10.1177/14680874241260762

Interactions of row blades of a marine compressor based on POD analysis

Huabing Lu [a,b], Youhong Xiao [a,*], Zhigang Liu [a], Ye Yuan [a], Peilin Zhou [b,*]

[a] College of Power and Energy Engineering, Harbin Engineering University, Harbin, China.
[b] Department of Naval Architecture and Marine Engineering, University of Strathclyde, Glasgow, United Kingdom.

Author affiliations:

Huabing Lu, Institution: Harbin Engineering University and University of Strathclyde. Address: NO.145-1 Nantong Street, Nangang District, Harbin City, Heilongjiang Province, China. Email: luhuabing@hrbeu.edu.cn.

Youhong Xiao, Institution: Harbin Engineering University. Address: NO.145-1 Nantong Street, Nangang District, Harbin City, Heilongjiang Province, China. Email: xiaoyouhong@hrbeu.edu.cn.

Zhigang Liu, Institution: Harbin Engineering University. Address: NO.145-1 Nantong Street, Nangang District, Harbin City, Heilongjiang Province, China. Email: liuzhigang@hrbeu.edu.cn.

Ye Yuan, institution: Harbin Engineering University. Address: NO.145-1 Nantong Street, Nangang District, Harbin City, Heilongjiang Province, China. Email: yuanye1@hrbeu.edu.cn.

Peilin Zhou, Institution: University of Strathclyde. Address: 16 Richmond Street, Glasgow G1 1XQ, United Kingdom. Email: Peilin.zhou@Strath.ac.uk.

[*] Corresponding author
Email: xiaoyouhong@hrbeu.edu.cn (Yonghong, Xiao), Peilin.zhou@Strath.ac.uk (Peilin, Zhou).

Abstract

The complex internal flow of the marine Low-Pressure Compressor (LPC) is characterized by a series of unsteady flow structures, presenting extensive temporal and spatial features that pose challenges to direct data analysis. This paper employs the Unsteady Reynolds-averaged Navier Stokes (URANS) method to simulate a marine 1.5-stage LPC with full-channel configuration. Validation of the compressor's overall characteristics and the unsteady pressure is achieved through comparison with experimental data. Additionally, the Proper Orthogonal Decomposition (POD) method is applied to decompose the velocity and pressure fields in various computational regions. The results demonstrate that the combined use of URANS and POD facilitates detailed insights into blade interactions. The consistency between time-averaged variables and POD modes underscores the practical physical significance of the POD modes. Furthermore, the study reveals that the Rotor-Stator interaction significantly outweighs the Inlet Guide Vane (IGV)-Rotor interaction. The coherent modal pairs generated by different interferences exhibit diverse characteristics within the computational domain, with distinct frequencies

observed for the same interference reaction in the upstream and downstream regions. Notably, the POD modes of the rotor pressure field unveil a separation bubble structure.

Keywords: Marine Low-Pressure Compressor; Proper orthogonal decomposition; Rotor-Stator interaction; Numerical simulation

1. Introduction

Within contemporary gas turbine systems, the Low-Pressure Compressor (LPC) emerges as an indispensable and intricate component, often posing formidable design challenges. Functioning as the primary constituent within the inlet section of the multistage axial compressor, the LPC assumes a pivotal role with far-reaching implications for the comprehensive aerodynamic performance of the entire compressor assembly [1]. When contemplating the operation of an engine in scenarios that deviate from the design conditions, it becomes evident that the internal flow characteristics within the LPC manifest the most pronounced disparities from their originally intended parameters. The LPC encounters numerous complex conditions. For instance, the low-speed cruising condition of the ship results in reduced LPC flow. Additionally, the LPC

must operate in a marine environment characterized by high humidity and high-salinity air. Consequently, the optimization of LPC performance stands as a mission of paramount significance, particularly in the context of applications germane to the realm of ship and ocean engineering. Such optimization holds the promise of substantially enhancing the overall efficiency of the gas turbine system, thereby underscoring its profound relevance and implications within this domain.

The internal flow of the LPC exhibits strong, three-dimensional, unsteady characteristics [2]. The main unsteady flows involve, e.g., the fan-intake interaction [3, 4], boundary layer separation [5-7], radial separation [8, 9], tip leakage [10, 11], rotor vortex shedding [12, 13], blade-wake interaction [14], and rotor-wake and stator interaction [15, 16]. The pressure distribution on the blade surface and flow loss are significantly influenced by these complex flows, thereby impacting the overall efficiency of marine gas turbines. A considerable body of work has been dedicated to describing the complex flow inside compressors. Cao et al. [3] conducted a qualitative study of the mechanism of the fan-intake interaction based on the Unsteady Reynolds-averaged Navier Stokes (URANS) and investigated the impact of distortion

on key design parameters of the intake. The isentropic Mach number distribution of the air intake showed that the fan could accelerate the flow upstream, thereby reducing the level of distortion near the fan. Gaetani et al. [15] studied the effect of the rotor on the flow released by the stator. The results showed that the rotor would periodically perturb the pressure and velocity fields of the gap between rotor and stator, which eventually led to the oscillation of the total pressure and temperature at the outlet. Gao et al. [17] pointed out that for various non-uniform tip clearance configurations, the tip load distribution had a significant impact on tip leakage flow. A non-uniform tip clearance configuration could alter the distribution of tip leakage flow. Different non-uniform tip clearances had diverse effects on the turbine, among which the front step and the shrinkage clearance reduced the total loss of the turbine.

These complex flows are often accompanied by a wide range of temporal and spatial features, which are coupled together so that the flow contains a lot of cluttered information [18]. Direct analysis of variables concerning space and time remains a challenge for even the simplest flows. Extracting key physical features or patterns of the flow is, therefore, a valid

means for in-depth analysis of complex flows. Reduced-order models provide a way to describe high-dimensional flows in a low-dimensional form [19], and Proper Orthogonal Decomposition (POD) is the most widely used in flow analysis.

POD is considered one of the most efficient methods for capturing the main components of an infinite-dimensional flow. Consequently, it is favored for a variety of applications, such as simple in-pipe flow, cavity flow, wing-wake, and high-speed jets. Shim et al. [20] adopted Particle Image Velocimetry (PIV) to study the structural characteristics of the planar jet during the development process and verified the existence of counter-rotating vortices in the initial region based on POD. The results showed that the characteristic frequency of the antisymmetric vortex was independent of the jet flutter. The symmetric vortex was gradually displaced relative to the flow direction and finally evolved into an anti-symmetric vortex. Zhao et al. [21] found that the aerodynamic performance of the airfoil was improved by the presence of leading-edge protuberances, attributed to the alteration in the momentum transfer process and flow transition mechanism within the spanwise laminar separation bubble at the

airfoil leading edge. The improved airfoil effectively suppressed the corresponding vortex shedding process. Murray and Ukeiley [22] processed PIV data for shallow rectangular cavity flow. The results showed that as the number of included POD modes increased, the absolute difference between the repair vector and the original PIV data approached the experimental uncertainty.

POD technology has also been applied to turbomachines. Cizmas and Palacios [23] modeled the flow field inside a single-stage turbine based by URANS. The phase-space diagram indicated the existence of low-dimensional dynamics, which supported the validity of the low-order model of the turbine. Sajadmanesh et al. [24] also used URANS to study the flow separation and reattachment on the suction side of the low-pressure turbine. The separation of bubbles on the blade surface under two working conditions was investigated using the POD technology. The results indicated that, high-energy, large-scale structures at low Reynolds numbers were detached from the separation shear layer. Conversely, low-energy, small-scale structures at high Reynolds numbers were observed in the separation zone and downstream of the trailing edge. Luo [25] proposed a

POD-based hybrid model approach to optimize the aerodynamic design of a low-speed 4.5-stage compressor while maintaining mass flow by modifying the spanwise dislocation angle and curvature of the stator blades. It was demonstrated that the hybrid model based on POD was an effective and feasible method in aerodynamic optimization design. Moghadam et al. [14] conducted spatiotemporal and modal analyses of tip vortex systems in ducted axial fans under on-design and off-design conditions. The interaction patterns captured by the POD were consistent with eigenfrequencies in the fan noise spectrum. The blade-wake and multi-frequency interaction were more severe under the off-design condition with a larger tip clearance configuration.

The research described demonstrates that a combination of the URANS and POD can be utilized to extensively investigate complex flows within turbomachinery. Gaining insight into the vortex structures of different scales within the marine LPC offers a fresh perspective for developing techniques to control complex flow, thus reducing the flow loss of the entire compressor and maritime gas turbine. However, research on the Rotor-Stator interaction of turbomachinery using the POD method is

scarce, particularly concerning 1.5-stage axial compressors. The marine 1.5-stage axial compressor features three rows of blades, including guide vane, rotor, and stator, leading to diverse interference effects among multiple blade rows. Currently, the various interference characteristics of multistage axial compressors are not sufficiently understood. Therefore, initiating the study with the marine 1.5-stage axial compressor as the focal point is considered a prudent choice.

In this paper, POD was used to study the interactions of the marine 1.5-stage LPC. The POD of the velocity field was used to identify upstream wakes and detect downstream interactions, while the POD of the pressure field was adopted to study upstream interactions. The results show that the combination of the URANS and POD methods can successfully identify the interference between the compressor's blade rows. The physical significance of the POD modes is argued and strengths of different interferences are discussed in detail.

In this paper, the interactions of the marine 1.5-stage LPC are studied using POD. The decomposition results of the velocity field are utilized to identify the upstream wakes and its interaction with the downstream blade,

whereas the decomposition results of the pressure field were employed to capture the influence of downstream interference on the upstream. The results demonstrate that the URANS and POD in combination can effectively identify the interference between the blade rows of compressor. The physical significance of the POD modes is discussed, and the strengths of different interferences are detailed.

2. Numerical simulations

2.1. Marine compressor configuration

The marine LPC examined in this paper is a 1.5-stage subsonic axial flow compressor situated at Harbin Engineering University, China. It comprises three rows of blades: the Inlet Guide Vane (IGV), the rotor, and the stator, as depicted in Fig. 1. Operating at a speed of 2270 rpm, the compressor generates a flow rate of 3.8 kg/s and operates with an efficiency of 84.9%. Additional parameters of the marine compressor are detailed in Table 1.

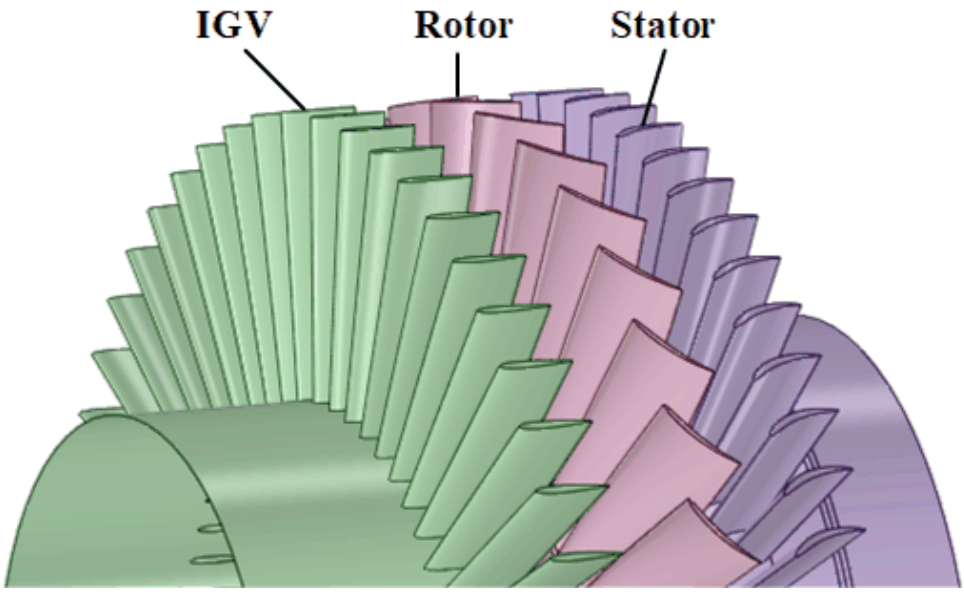

Fig. 1. Schematic diagram of the impeller.

Table 1.

Configuration of the marine compressor.

Inlet/Outlet shroud diameter D1	458.4 mm
Inlet hub diameter D2	243.6 mm
Outlet hub diameter D3	279 mm
Number of guide vanes	54
Number of rotors	37
Number of stators	60
Tip clearance	0.5 mm

2.2. Computational grid and boundary condition

The structured hexahedral elements of the compressor are generated

using the multi-block approach, as illustrated in Fig. 2. Fig. 2(a) depicts the CFD computational regions, which includes the IGV, rotor, and stator regions. Fig. 2(b) presents a schematic diagram of the grid divided into O4H structured hexahedral elements. Fig. 2(c) displays a partial grid diagram of the three-row blades surface, highlighting the distinct structural elements. Autogrid5 of NUMECA is employed to generate the structural elements of turbomachinery, which facilitates the creation of high-quality structured hexahedral elements. The mesh topology of the throughflow domain is O4H, while a perfectly matched butterfly mesh is adopted in the tip clearance. Due to the compact structure of the axial compressor, the middle rotor blades and the front and rear rows of blades form highly staggered configurations. To improve grid quality, C-type topological blocks based on O4H topology are defined both upstream and downstream of the rotor blades. The IGV region extends upstream from the leading edge by 2 times the IGV chord length C_{IGV}, while the stator region extends downstream from the trailing edge by 1.5 times the stator chord length C_S.

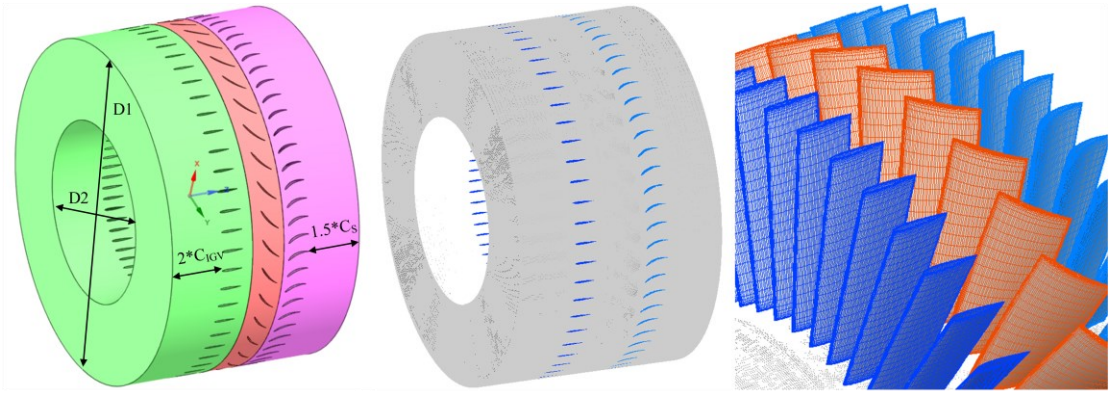

(a) Computational regions (b) Computational grid (c) Blades grid

Fig. 2. Computational domain and grid.

The overall characteristics of the marine compressor can be described by the pressure ratio π and efficiency Eff, which are defined as

$$\pi = \frac{P_{out}}{P_{in}} \tag{1}$$

$$Eff = \frac{\pi^{\frac{k-1}{k}} - 1}{\frac{T_{out}}{T_{in}} - 1} \tag{2}$$

where P_{out} and P_{in} are the total pressure of the outlet and the inlet, respectively, and k is the specific heat ratio of air. T_{out} and T_{in} are the outlet and inlet total temperature, respectively. Three different grid schemes are investigated to explore the effect of the element density on the numerical results. The total number of elements for Grids 1, 2, and 3 are 18, 27, and 36 million, respectively. Fig. 3 shows the efficiency curves for the three grid schemes as a function of flow. The calculation results of

Grids 2 and 3 are relatively close. Grid 2 is proved to meet the grid-independence requirement and adopted for all subsequent numerical simulations. The grid height of the first layer of the wall is set to 3×10^{-6} m and the steady simulation y+ results are shown in Fig. 4. The results fulfill the requirements of the shear stress transport (SST) turbulence model [24, 26] for all areas excluding a small region at the leading edge of the rotor and stator where y+ > 1.

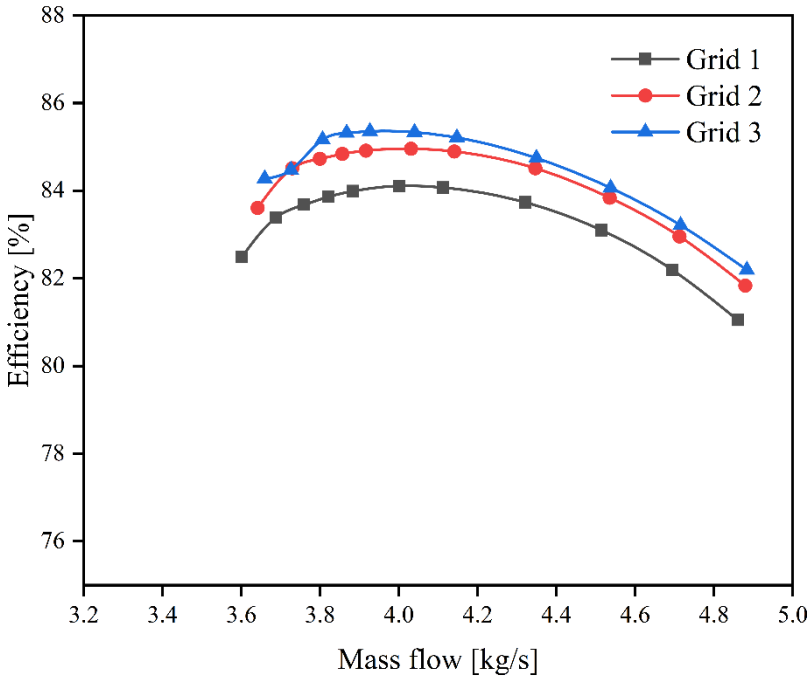

Fig. 3. Grid independence verification.

The total pressure at the inlet is atmospheric, with 101325 Pa, while the total temperature is 288.15 K. The flow direction of inlet is set normal to boundary, and turbulence intensity of inlet is medium, with 5%

turbulence intensity. The outlet static pressure is specified based on radial averages, and the wall boundary conditions are set to no-slip and adiabatic, except for the shroud wall corresponding to the top of the rotor, which is set as a counter-rotating wall because the actual wall not rotate with the rotor blades. The boundary conditions for the calculation domains of the marine compressor are depicted in Fig. 5. In the steady-state simulation, the data exchange type of the interface where different regions overlap is set to Mixing-Plane, which is changed to Transient Rotor-Stator for unsteady simulations.

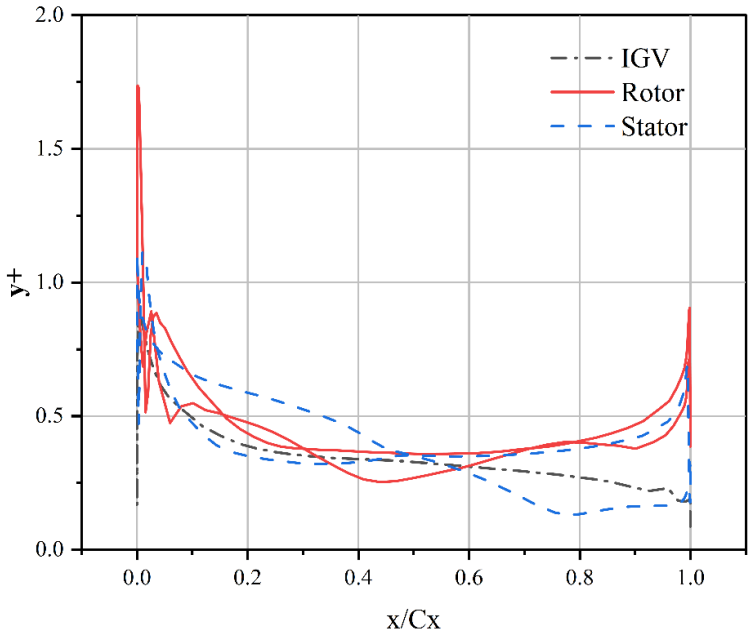

Fig. 4. The wall normal grid resolution of the blades.

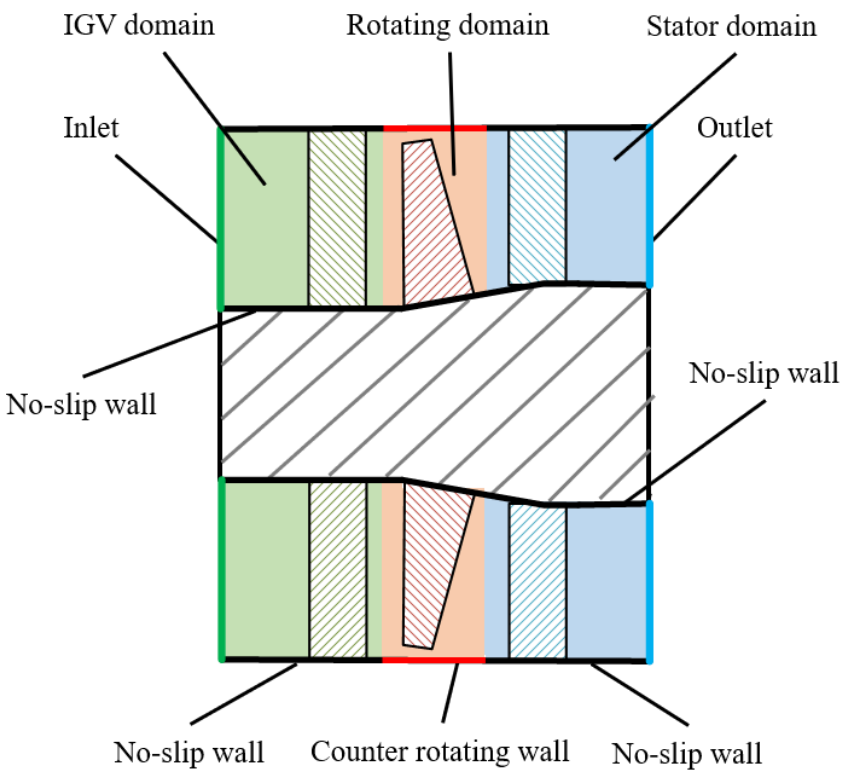

Fig. 5. The boundary conditions of the marine compressor.

2.3. Numerical solution method

The full-loop numerical simulation of the 1.5-stage axial compressor is conducted using CFX, employing the finite volume method to solve the Navier-Stokes equations. The SST turbulence model, a typical low Reynolds number model within the Reynolds-averaged Navier-Stokes (RANS) framework, is utilized. The SST model can accurately capture flow phenomena near the blade surfaces, such as separation flow caused by adverse pressure gradient. Due to this capability, the SST model is

widely used in the numerical simulation of turbomachinery [27, 28]. For the steady simulation, the convection scheme and turbulence accuracy are set to high resolution. For unsteady simulation, the initial values are specified using the results from the steady calculation, and the transient scheme is second-order backward Euler. The time step is mainly determined by the physical precision, which in this case is implemented as 40-time steps for one rotor channel, corresponding to 1.78593×10^{-5} s.

3. The POD method

POD is a popular method for reducing fluid dimensionality, providing an algorithm to decompose a series of data into an orthogonal basis of spatially correlated modes [18, 21] while capturing as much energy as possible. Upon completing the flow calculation described in Section 2, POD is employed to extract the flow modes. Given that the spatial dimension is significantly larger than the time dimension, the snapshot POD method is utilized in this paper.

A snapshot data set $X_{n\times m}$ of the study variables must be collected, which contains n rows and m columns, where n represents the number

of spatial nodes in the research area and m represents the number of consecutive temporal snapshots, and is given by

$$X = \left\{ x_1\left(x,t_1\right), x_2\left(x,t_2\right), x_3\left(x,t_3\right), \cdots x_m\left(x,t_m\right) \right\} \tag{3}$$

where x_i is the i-th flow-field snapshot with n spatial nodes. The goal of POD analysis is to find the optimal basis vectors that can represent the given data, that is, to find the vector that can represent X optimally in terms of energy. The solution to this problem [29] can be implemented by finding the following eigenvectors and eigenvalues

$$R\psi_j = \lambda_j \psi_j, \tag{4}$$

where $R = X^T X$ is a square matrix of size $m \times m$, ψ_j and λ_j represent eigenvectors and eigenvalues, respectively. When n is much larger than m, the characteristic value problem of $n \times n$ is reduced to $m \times m$, which greatly reduces the amount of computation. The eigenvalue problem associated with the eigenvector ψ_j is specified and the POD modality is recovered as

$$\phi_j = \frac{\sum_{i=1}^{m} \psi_j^i x_i}{\left\| \sum_{i=1}^{m} \psi_j^i x_i \right\|} \tag{5}$$

where $\|\cdot\|$ represents the L^2 norm. X can be decomposed orthogonally as

$$X = \sum_{j=1}^{m} a_j \phi_j , \tag{6}$$

where ϕ_j is the POD mode and a_j is the corresponding coefficient, such that the time coefficient a_j is given by

$$a_j = \phi_j^T x_j . \tag{7}$$

The original flow field can be reconstructed by Eq. (4) using the POD modes and corresponding coefficients. The instantaneous field can be reconstructed with only a few modes of interest and the most dominant flow mode is found. In addition, the eigenvalues λ_j in Eq. (2) represent the amount of energy contained in the corresponding mode. Sorting the results according to the size of the eigenvalues can distinguish the energy contained in the POD mode and the ratio of each mode to the total energy can be obtained. A more detailed introduction to the POD method and its applications is reported in other work [19, 30-32]. In this paper, two physical quantities, velocity and pressure, inside the marine compressor are extracted as snapshots for the POD analysis.

4. Results and discussion

4.1. Compressor flow characterization and verification

To describe the accuracy of the simulation, the relative deviation ε is defined as

$$\varepsilon=\frac{\left|\theta_{num}-\theta_{\exp}\right|}{\theta_{\exp}} \tag{8}$$

where θ_{num} and $\theta_{\exp}$ are the numerical and the experimental values of the research variables, respectively. The two predominant flow characteristic variables in this paper are the pressure ratio π and efficiency Eff of the compressor. The pressure ratio and efficiency of the marine compressor and their relative deviations are shown in Table 2. The absolute values and relative deviations are provided, with the relative deviations of the pressure ratio and efficiency being 0.218% and 0.225%, respectively. This demonstrates that the numerical results align well with the experimental data, thereby validating the numerical scheme employed. To further verify the accuracy of the unsteady simulation, high-frequency dynamic pressure probes are arranged in the rotor tip clearance. The corresponding test bench conditions and measurement positions refer to [33].

The location of the dynamic pressure measurement points and the frequency characteristics of the unsteady pressure at the tip clearance are depicted in Fig. 6, which illustrates the high-frequency dynamic pressure probes XT-140 (M) Kulit positioned at the leading edge of the rotor blades. These probes feature a pressure range of 1.7 mbar, a sensitivity of 2.301 mV/mbar, and a sampling frequency between 150 kHz and 240 kHz, ensuring dynamic pressure measurement accuracy in high-speed compressors. The close agreement between the frequency characteristics obtained through simulation and experiment confirms the accuracy of the simulations.

Table 2.

Characteristics of the marine compressor obtained through experiment and numerical simulation.

Results	π	Eff (%)	ε_{π} (%)	ε_{Eff} (%)
Experimental	1.0089	84.919	–	–
Numerical	1.0111	84.728	0.218	0.225

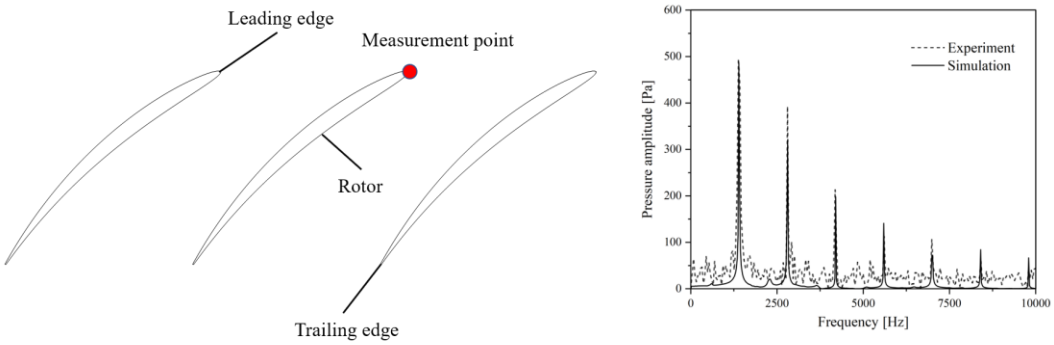

(a) The location of dynamic pressure measurement point

(b) Compressor unsteady pressure verification

Fig. 6. Measurement point and pressure verification.

4.2. Time-averaged flow characteristics

Before performing POD analysis, it is necessary to ensure that the number of POD snapshots does not affect the analysis results. For this study, 400 and 800 snapshots of the stator pressure at 50% span are extracted for POD analysis, with the results shown in Fig. 7. Given that the time step for unsteady simulations is 1.78593×10^{-5} s, it takes 40-time steps for the rotor blades to rotate through the angle corresponding to a single rotor passage. During compressor output, data are recorded at intervals of two-time steps, so 800 snapshots corresponded to a physical time slightly exceeding one revolution of the compressor, which is sufficient to ensure that the POD analysis results are unaffected. For 400 snapshots, data are recorded at intervals of four-time steps, resulting in the same physical time as 800

snapshots but with twice the time interval between snapshots. In terms of resolution, 800 snapshots guaranteed 20 sampling points in a rotor channel, ensuring high-precision time resolution. The energy fractions obtained using 400 snapshots are almost identical to those of 800 snapshots, as shown in Fig. 7, indicating that 400 snapshots meet the requirement for quantity irrelevance. To eliminate the influence of the number of snapshots on the results, the present paper discusses the results obtained using 800 snapshots. Additionally, the first four-order modes are the most dominant, with their combined energy accounting for 96.8% of the total flow energy.

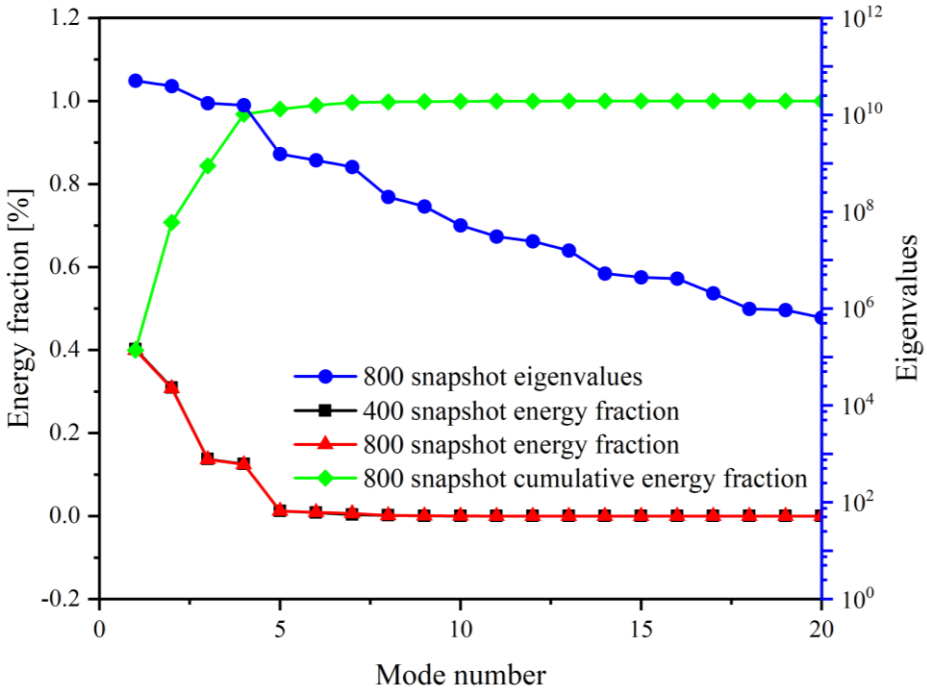

Fig. 7. POD eigenvalues and energy fraction.

To avoid the influence of complex flows near the rotor root and tip, 50%

span is selected as the position for POD analysis. The POD analysis is conducted on the velocity magnitude of the three rows of blades to elucidate the flow characteristics from the perspective of flow energy, located at half the span of the blades, as shown in Fig. 8. Specifically, the POD analysis is applied to the three turbomachinery surfaces, encompassing a total of 569,805 spatial points. Furthermore, the POD modes obtained from the solution are normalized to ensure the results fell within the range of [-1, 1] in the present study.

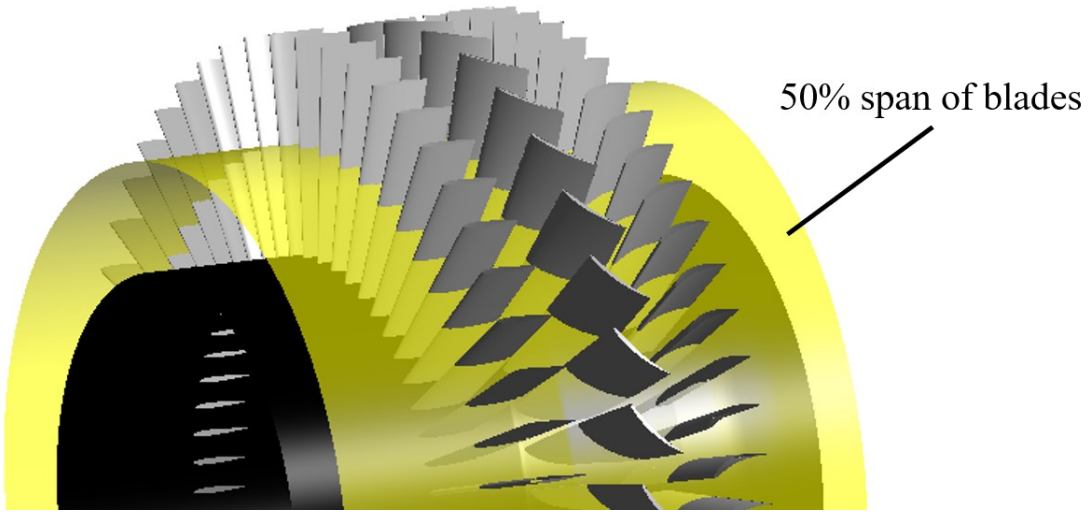

Fig. 8. Location of POD slice for interaction of blades.

To facilitate a clearer understanding of the POD modes, the time-averaged variable characteristics within the compressor are presented initially. Given that mode 1 dominates the flow energy, the investigation of flow characteristics focuses on mode 1. Fig. 9 presents a comparison

between mode 1 of POD and the distribution of time-averaged velocity at the 50% span of the compressor. It is evident that the spatial distribution of mode 1 closely matches the time-averaged velocity distribution. Additionally, the temporal behavior of mode 1 is quite stable across the three cross sections, as illustrated in Fig. 10. Therefore, mode 1 represents the average unsteady flow velocity within the compressor and contains the most kinetic energy.

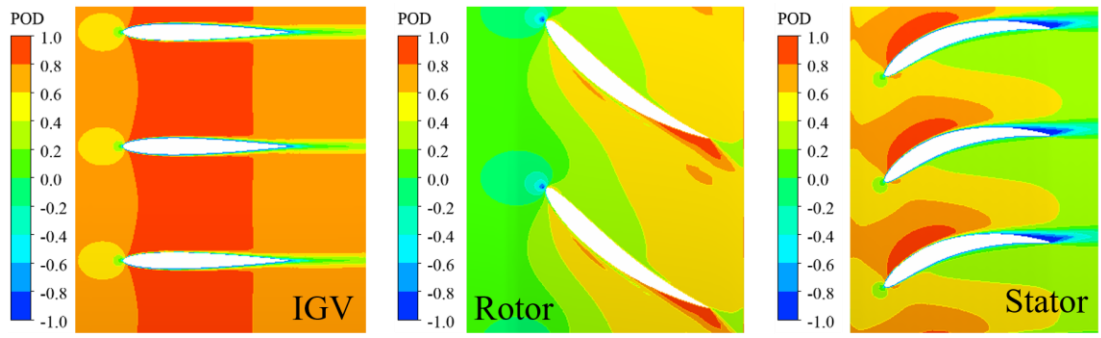

(a) Mode 1 of POD in 50% span

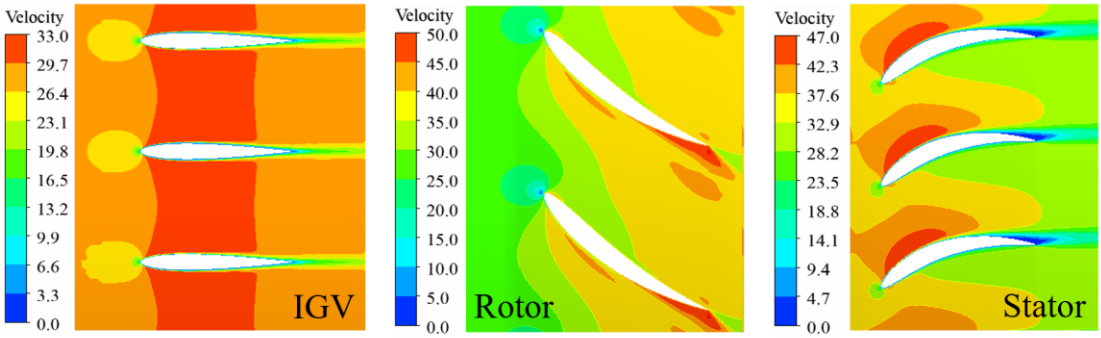

(b) Distribution of time-averaged velocity in 50% span

Fig. 9. Comparison of mode 1 and time-averaged velocity.

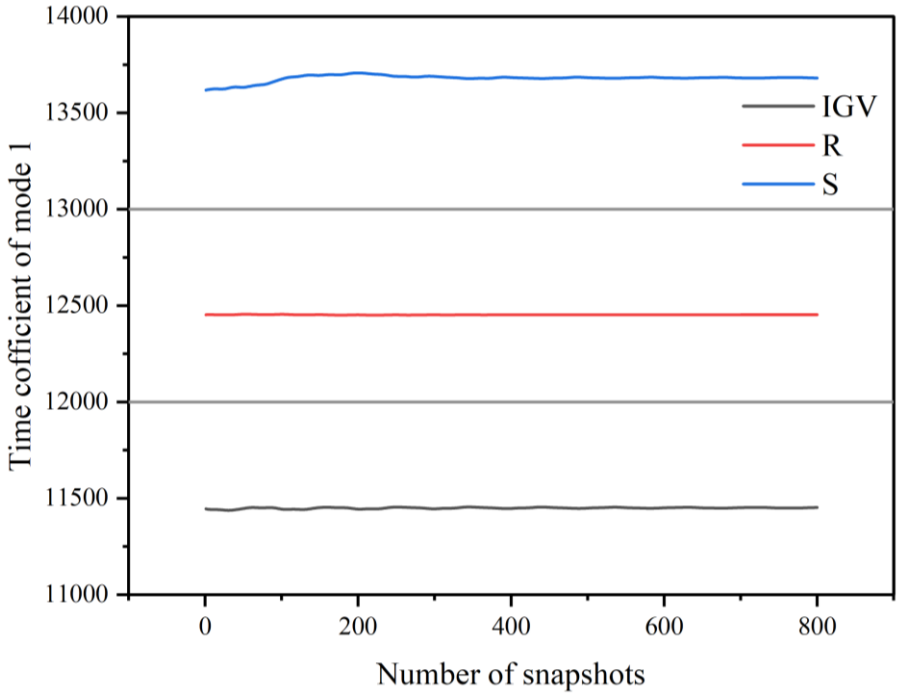

Fig. 10. The time-varying process of mode 1.

Fig. 11 and Fig. 12 illustrate the higher-order POD modes and helicity distribution of the rotor and stator, as defined by Eq. (9). Helicity describes the vortex distribution on the turbo surface and can also represent separated flow in the boundary layer. Modes 2 and 3 of the rotor and stator are similar to the corresponding helicity distribution, as evidenced by the flow structures in circles A and B in the figures. The flow structures in Fig. 11(c) and Fig. 12(c) develop from upstream, propagating from the IGV-Rotor interface and Rotor-Stator interface downstream, passing through the blade channel, and finally mixing with the blade wakes for dissipation. Therefore, the helicity in circles A and B represents the wakes of upstream blades,

indicating that the higher-order modes of the rotor and stator describe the propagation and dissipation of upstream blade wakes in the downstream domain. The flow structure in circle C in Fig. 11 represents the separated flow and wake of the rotor, although higher-order modes can only capture subtle flow eddies. The higher-order modes in the rotor region primarily recognize the wakes of the IGV, and accordingly, the wakes of the rotor are captured by the higher-order modes in the stator domain. The results indicate that the higher-order modes obtained from the POD of velocity predominantly recognize upstream characteristics, while it is challenging to capture downstream flow characteristics.

$$Helicity = (\nabla \times \vec{V}) \cdot \vec{V} \tag{9}$$

where $\vec{V}$ is the velocity.

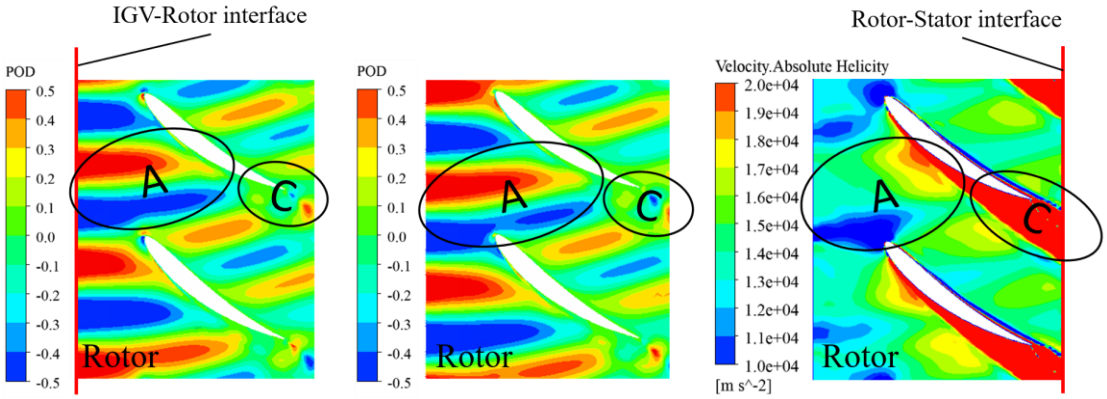

(a) Mode 2 (b) Mode 3 (c) Distribution of helicity

Fig. 11. Interpretation of higher-order modes of rotor.

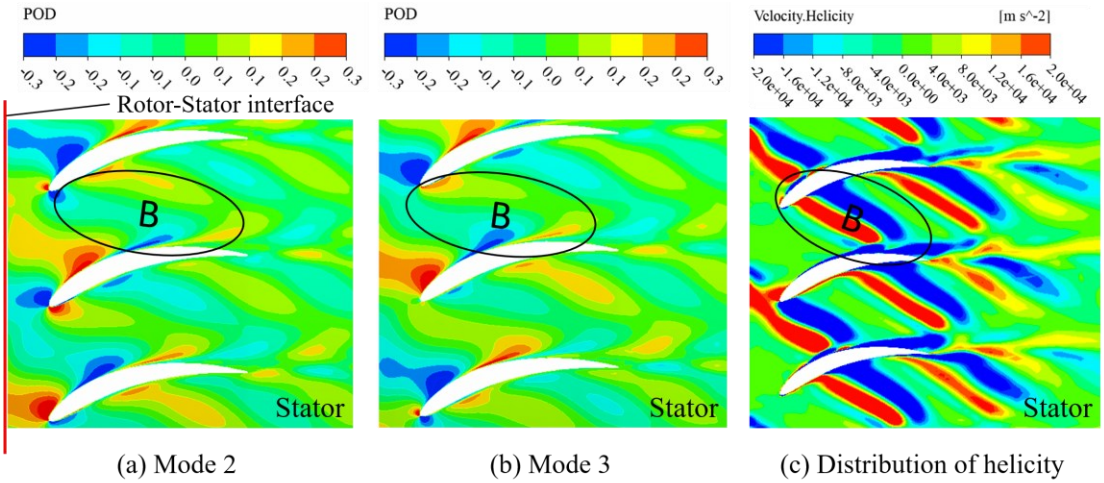

(a) Mode 2 (b) Mode 3 (c) Distribution of helicity

Fig. 12. Interpretation of higher-order modes of stator.

4.3. Fluctuating flow characteristics and velocity POD analysis

From the preceding discussion, it is evident that only the higher-order modes of POD can reflect the blade wakes for interaction analysis, whereas mode 1 of POD solely represents the average flow, excluding the interaction between blades from the average flow. In contrast to Section 4.2, only the fluctuating velocity is utilized for POD analysis in this section. Consequently, mode 1 no longer represents the average flow, but is equivalent to mode 2 in the previous section. Similarly, the fluctuating velocity on the three turbomachinery surfaces is extracted for POD analysis, and the energy proportions of the modes are depicted in Fig. 13. The energy distribution of POD modes on the three surfaces exhibits similarity. The

combined energy of the first two- and four-order modes accounts for at least 73.3% and 88.8% of the total kinetic energy, respectively. Hence, the first four-order modes are the focal point of this analysis.

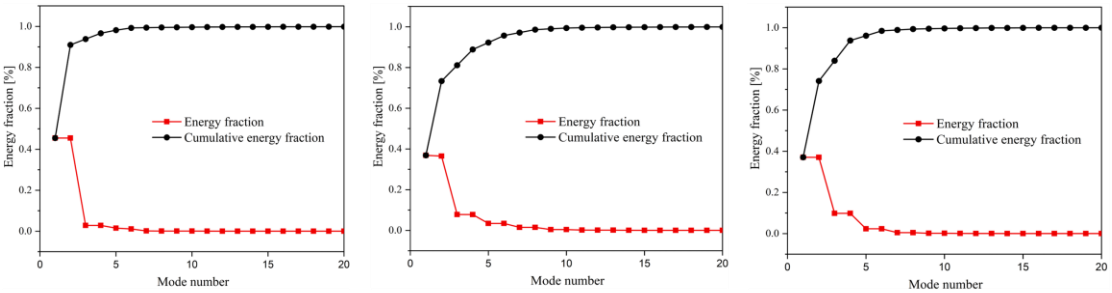

(a) IGV (b) Rotor (c) Stator

Fig. 13. Proportion of mode energy in different computing domains.

In conjunction with Fig. 11 and Fig.12, Fig. 14 to Fig. 16 present the spatial distribution of the first four-order modes of POD on the three turbomachinery surfaces. It is evident that mode 1 and mode 2 form a coherent pair of modes, as indicated by their similar spatial distribution, with their equal energy fraction shown in Fig. 13. Similarly, mode 3 and mode 4 constitute another coherent pair of modes. Concerning the POD modes of the IGV, the first two-order modes are only generated near the IGV-Rotor interface. Modes 1 and 2 thus depict the behavior of the IGV-Rotor interaction in the upstream IGV domain. Conversely, modes 3 and 4 capture the vortex structures of the IGV wakes, comprising a pair of opposing vortices that develop downstream with a slight interaction

observed at the IGV-Rotor interface, as highlighted by the red circle in the figure.

For the rotor and stator, the first two-order modes primarily depict the interaction of the upstream blade wakes with the downstream blades, as discussed in the previous section. Modes 3 and 4 indicate that the number of wakes is approximately twice that of the first two-order modes, resulting in a dominant peak frequency twice as high as expected for modes 1 and 2. Additionally, the interference range of modes 1 and 2 encompasses the entire computational region, as the wakes of the upstream blades experience no significant attenuation in the channel and are able to propagate to the Rotor-Stator interface, while modes 3 and 4 decay continuously in the channel. This implies that high-frequency flow interaction can hardly cross downstream blades and interfere with blades further downstream, whereas lower-order modes may cross adjacent blades and interact with blades further downstream.

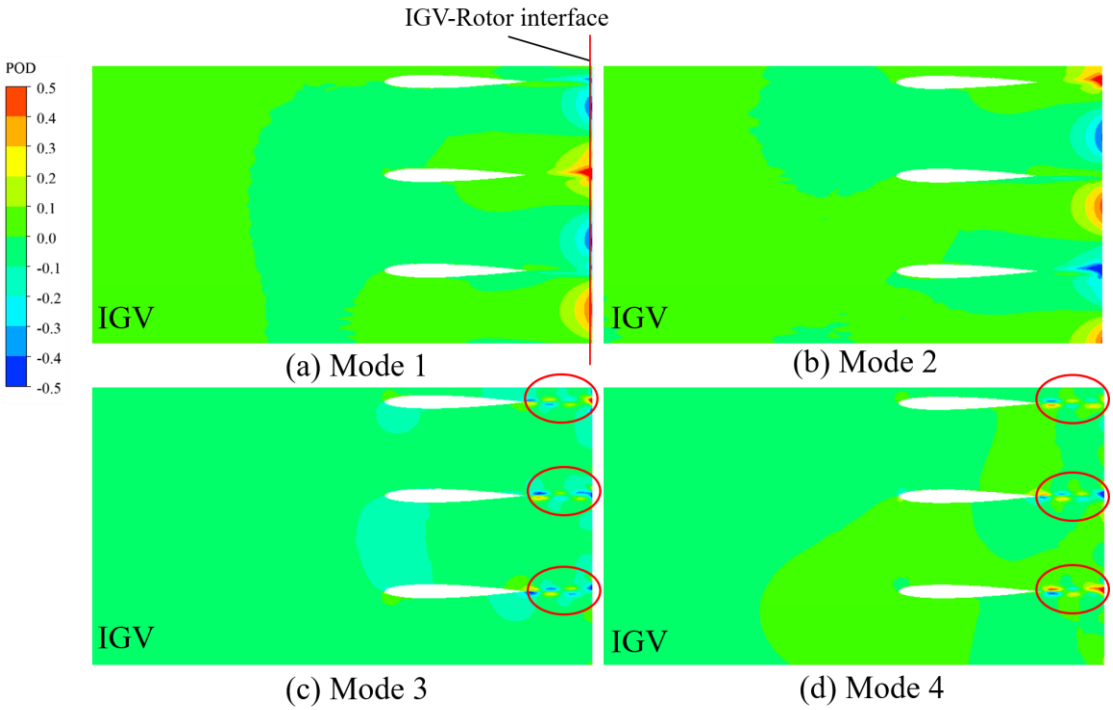

Fig. 14. The velocity POD modes of the IGV.

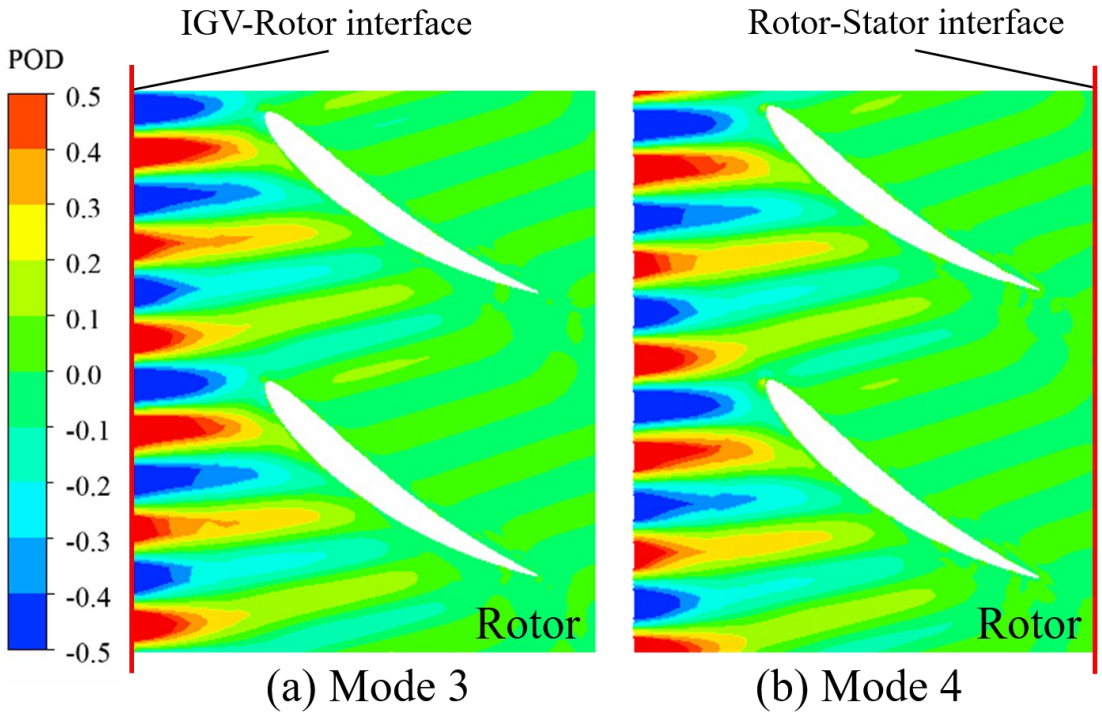

Fig. 15. The velocity POD modes of the rotor.

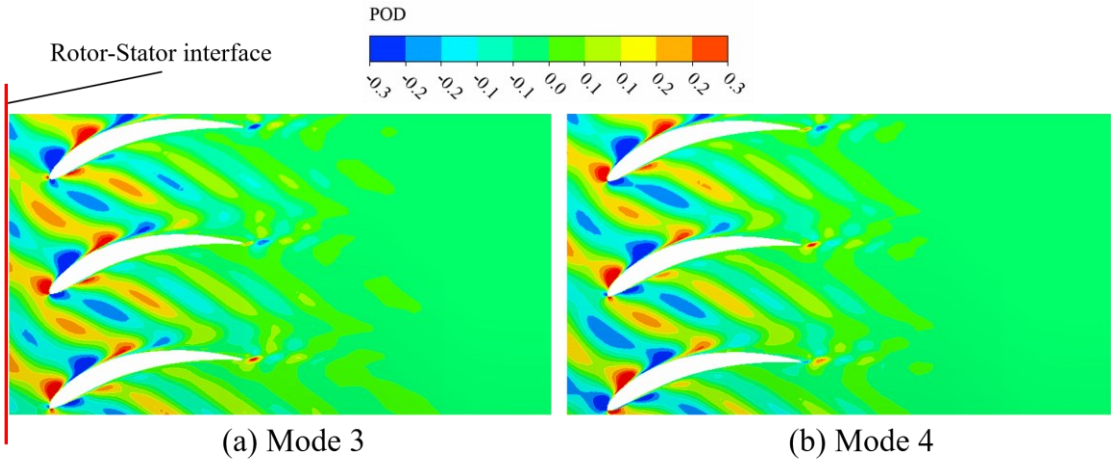

Fig. 16. The velocity POD modes of the stator.

Since the coefficients of the POD modes reflect the time evolution process, the time and frequency information of each mode can be extracted to further elucidate the interaction mechanism. For the first four-order modes on the three turbomachinery surfaces, the frequency characteristics are obtained by Fourier transform of their time coefficients, as illustrated in Fig. 17. The mode peaks of the IGV are concentrated on the Blade Pass Frequency (BPF, 1400Hz) and its harmonics. Specifically, the first two-order modes oscillate mainly at the BPF, while modes 3 and 4 oscillate at twice the BPF. The BPF and its harmonic frequencies are described by

$$f = \frac{nBi}{60}, \tag{10}$$

where n is the rotor speed, B is the number of rotor blades, and i is the harmonic order. The fact that the frequency obtained by taking the

number of rotor blades from *B* matches the peak frequency of the IGV mode proves that the IGV modes are the reflection of the interaction in the upstream IGV region between IGV wakes and rotor blades.

The peak frequencies of its POD modes coincides with the Vane Pass Frequency (VPF, 2043Hz) in the rotor region, which is determined using Eq. (10). Unlike the BPF, the *B* in Eq. (10) should represent the number of IGVs. This finding is in line with the earlier analysis, indicating that the POD modes in the rotor region primarily indicate that the rotor blades are influenced by the wakes of 54 upstream IGVs. Similarly, for the stator POD modes, the stator blades are influenced by the wakes of 37 rotors. The interaction with the wakes of 37 rotors inevitably leads to the modal frequency peaks of the stator being the BPF and its harmonics. As anticipated, for both the rotor and stator, twice the number of wakes of modes 3 and 4 results in twice the dominant frequencies of modes 1 and 2, as depicted in Fig. 17(b) and Fig. (c).

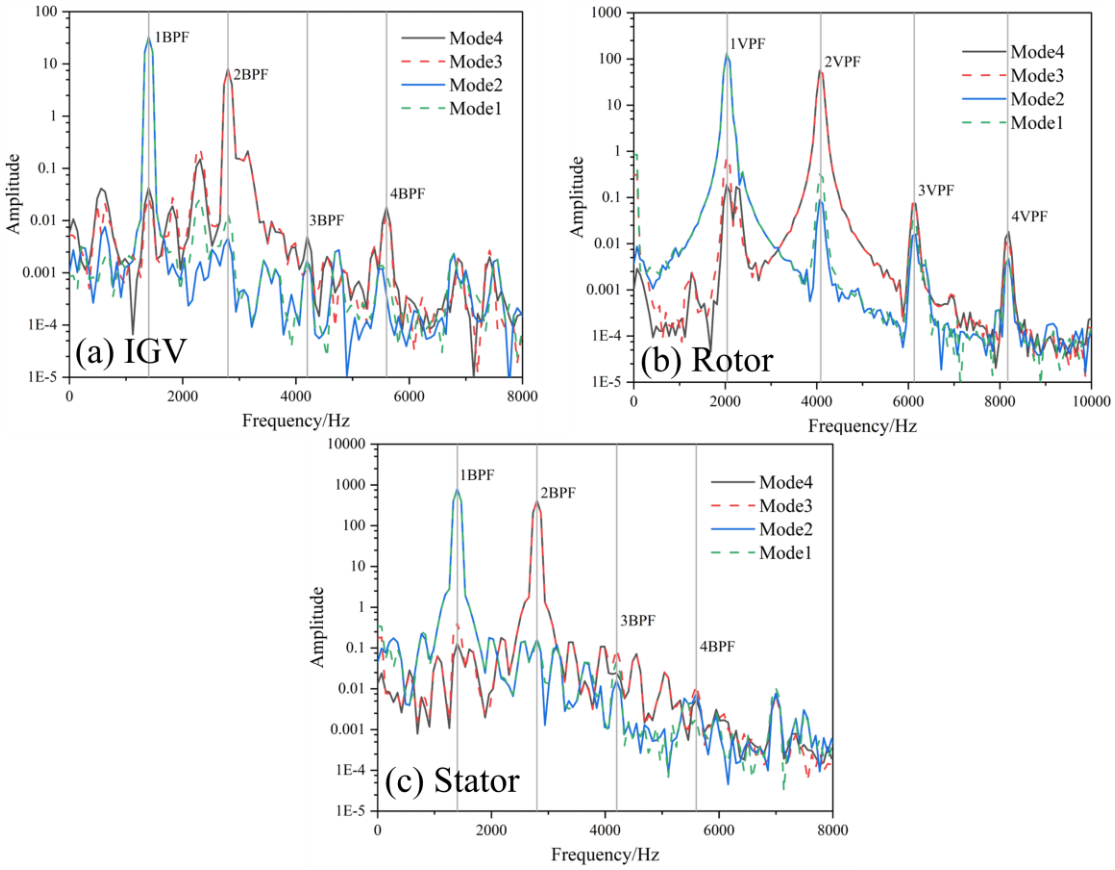

Fig. 17. Modes' frequency characteristics.

4.4. Interaction strength and pressure POD analysis

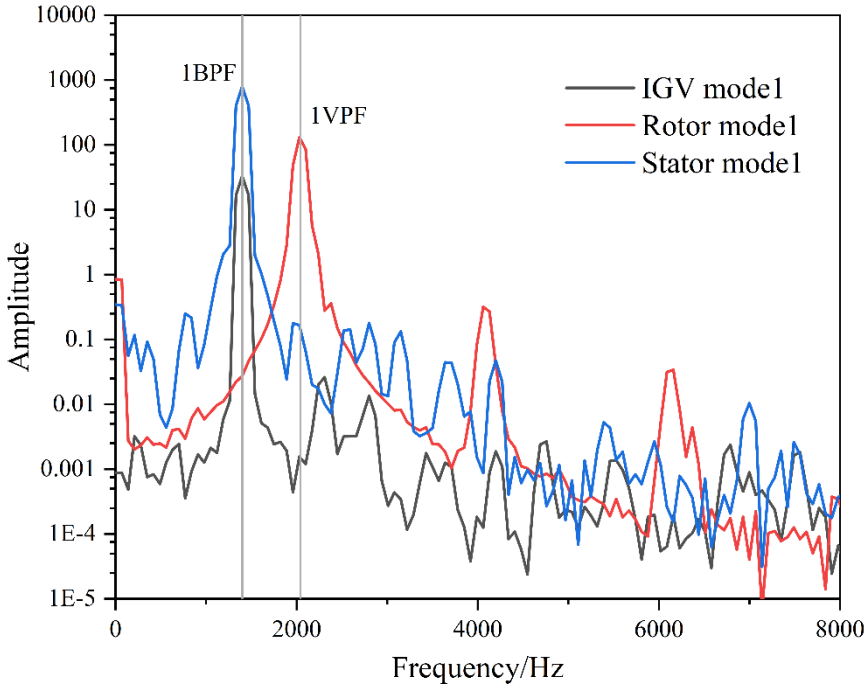

Fig. 18. Frequency characteristics of mode 1 in different domains.

Fig. 18 illustrates the frequency characteristics of mode 1 in different regions of the compressor. The stator region exhibits the largest amplitude, while the IGV region shows the smallest amplitude, with a disparity of about an order of magnitude between the regions. This discrepancy indicates that the strength of the Rotor-Stator interaction is significantly greater than that of the IGV-Rotor interaction. The POD results of the rotor velocity field, as presented in Fig. 11 and Fig. 15, do not exhibit the phenomenon of Rotor-Stator interference. This discrepancy may be attributed to the influence of the axial velocity component and the difficulty

in reflecting the interference effect in the stator region in the upstream region. Additionally, the rotor region encompasses the IGV wakes, which casts a shadow on the display of the Rotor-Stator interaction.

The POD modes of the 50% span pressure field of the rotor are depicted in Fig. 19. The energy proportions of the first four-order modes of the pressure field exhibit similarity, with the energy fractions of the coherent mode pairs, namely modes 1 and 2, and modes 3 and 4, amounting to 53.6% and 37.9%, respectively. The first coherent mode pair (modes 1 and 2) primarily represents the Rotor-Stator interaction in the upstream region, as indicated by their patterns concentrating on the Rotor-Stator interface. Their peak frequencies occur at 2270Hz, coinciding with the Stator Pass Frequency (SPF) obtained by adjusting the number of blades to 60 in Eq. (10). This alignment indicates that modes 1 and 2 precisely capture the upstream manifestation of the interference effect of rotor wakes and 60 stators.

The second coherent mode pair (modes 3 and 4) mainly reflects the IGV-Rotor interference effect, as evidenced by the frequency characteristics shown in Fig. 19(b). Moreover, Fig. 19(b) reveals that

modes 1 to 4 exhibit prominent peaks at VPF and SPF, implying that the POD results of the pressure field differ from that of the velocity field. The former is unaffected by the axial velocity, enabling the simultaneous capture of upstream and downstream interference in the rotor region. The amplitudes of the first and second modal pairs are equivalent, indicating consistent interaction strength between the IGV-Rotor in the downstream pressure field and the Rotor-Stator in the upstream. Additionally, the second coherent mode pair generates a vortex mass on the rotor suction surface. This “separation bubble” is mentioned in the work of Sajadmanesh et al [24].

In summary, the POD modes of the velocity field can extract the main flow structure, but it is difficult to analyze the effect of the interaction on the upstream. The POD modes of the pressure field pay more attention to the pressure change which can overcome the defect of velocity field, but it is challenging to decompose the characteristic flow structure.

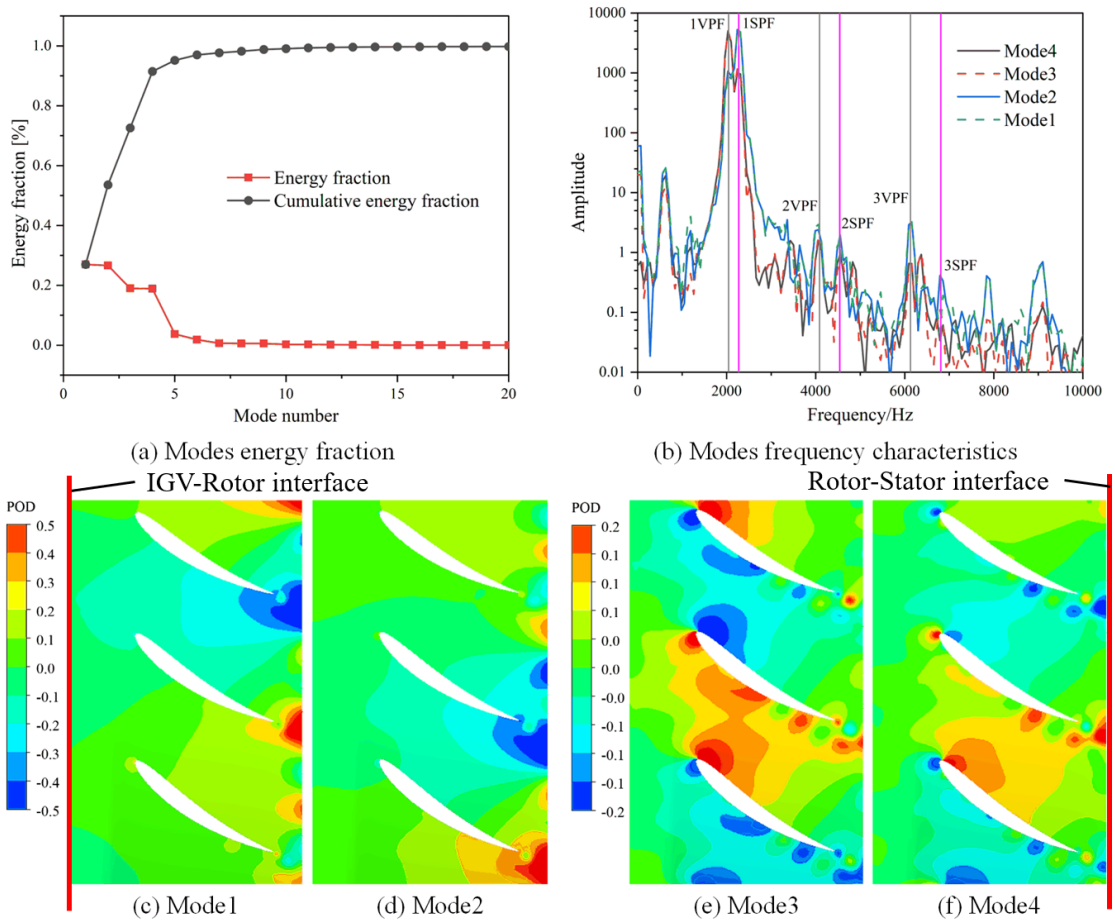

Fig. 19. The pressure POD modes at the 50% span of the rotor.

5. Conclusions

The interference characteristics and intensity magnitudes between multiple rows of blades in a marine 1.5-stage LPC are studied in detail using the POD. The SST turbulence model is used for the URANS calculation, and the accuracy of the simulation is verified by experimental data, including a comparison of the overall characteristics of the compressor. The insights derived from this investigation contribute to the

optimization of marine compressor performance and the enhancement of overall operational efficiency in maritime vessels. Consequently, this study offers a significant reference for future endeavors aimed at advancing flow optimization in the maritime domain.

POD results of velocity amplitude show that the first mode represents the average velocity of unsteady flow, and the higher-order modes reflect the flow structures of fluctuating velocity field. The higher-order POD modes in the rotor and stator regions describe the propagation and dissipation of upstream IGV wakes and rotor wakes in the downstream channel respectively.

The POD modes of the velocity field at the 50% span of the IGV identify the IGV-Rotor interaction and the IGV wakes composition. The modes representing the interaction and those representing the wakes have frequency characteristics related to the interference of the 37 rotor blades located downstream.

The POD modes of the rotor velocity field identify the existence of the IGV wakes and capture their interaction with the rotor blades and their downstream development. The oscillation frequency VPF of the rotor POD

modes is related to the impact of the upstream wakes on the rotor blades, that is, the manifestation of the IGV-Rotor interaction in the rotor region is identified. The rotor region does not reflect the Rotor-Stator interaction due to the axial velocity component and the shadowing effect of the IGV wakes. However, the POD modes of the rotor pressure field can simultaneously identify the IGV-Rotor and Rotor-Stator interactions, and the interference frequencies of the corresponding modes in the rotor region are VPF and SPF, respectively. Furthermore, the presence of a series of separation bubbles is found on the rotor suction surface.

The POD modes of the stator velocity field are similar to the results for the rotor and capture the interaction between the rotor wakes and the stator blades and the downstream development of the rotor wakes. At this time, the interference frequency of the Rotor-Stator interaction in the stator region becomes BPF, resulting from the continuous impact of the 37 rotor wakes on the stator blades.

From the POD results in the three regions, it is found that the frequency amplitude in the stator region is the largest, while that of the IGV is the smallest. The amplitudes of different regions differ by an order of

magnitude, which indicates that the strength of the Rotor-Stator interaction is much greater than that of the IGV-Rotor. Finally, all POD results reveal a common feature; modes 1 and 2 and modes 3 and 4 are two pairs of coherent paired modes and the frequency characteristics and energy fractions of coherent modes are consistent.

Declaration of Competing Interest

The authors declare no conflict of interest in preparing this article.

Acknowledgment

This work was supported by National Science and Technology Major Project (HT-J2019- || -0013-0034) and Fundamental Research Funds for the Central Universities (3072022TS0307).

References

1. Wang W, Chen L and Sun F. Thermodynamic optimization of a triple-shaft open intercooled, recuperated gas turbine cycle. Part 2: power and efficiency optimization. *International Journal of Low-Carbon Technologies* 2016; 11: 29-34. DOI: 10.1093/ijlct/ctt054.
2. Xiao X, McCarter AA and Lakshminarayana B. Tip clearance effects in a turbine rotor: Part I- Pressure field and loss. *Journal of*

Turbomachinery 2001; 123: 296-304. DOI: 10.1115/1.1368365.

3. Cao T, Vadlamani NR, Tucker PG, et al. Fan-intake interaction under high incidence. *ASME Turbo Expo: Turbine Technical Conference and Exposition*. Seoul, SOUTH KOREA2016.
4. Tian J, Sun Z, Chai P, et al. Study on the influence of inlet asymmetry on aerodynamic noise of cooling fan. *Journal of Engineering for Gas Turbines and Power-Transactions of the Asme* 2020; 142. DOI: 10.1115/1.4048449.
5. Gadzhiev DA and Gaifullin AM. Structure of laminar unsteady boundary layer separation under an airplane wake vortex interaction with a ground surface. *19th International Conference on the Methods of Aerophysical Research (ICMAR)*. Akademgorodok, RUSSIA2018.
6. Smith CJ and Mallier R. Removing the separation singularity in a barotropic ocean with bottom friction. *Journal of Computational and Applied Mathematics* 2004; 166: 281-290. DOI: 10.1016/j.cam.2003.09.027.
7. Wang Q, Luo H and Ma T. Boundary layer separation of 2-D incompressible dirichlet flows. *Discrete and Continuous Dynamical Systems-Series B* 2015; 20: 675-682. DOI: 10.3934/dcdsb.2015.20.675.
8. Ben M, Hall CA and Wilson MJ. Fan aerodynamics with a short intake at high angle of attack. *Journal of Turbomachinery-Transactions of the Asme* 2021; 143. DOI: 10.1115/1.4050606.
9. He X and Zheng X. Mechanisms of lean on the performance of

transonic centrifugal compressor impellers. *Journal of Propulsion and Power* 2016; 32: 1220-1229. DOI: 10.2514/1.B36008.

10. Du J, Lin F, Zhang H, et al. Numerical simulation on the effect of tip clearance size on unsteadiness in tip clearance flow. *Journal of Thermal Science* 2008; 17: 337-342. DOI: 10.1007/s11630-008-0337-x.
11. Zhang B, Mao X, Wu X, et al. Effects of tip leakage flow on the aerodynamic performance and stability of an axial-flow transonic compressor stage. *Energies* 2021; 14. DOI: 10.3390/en14144168.
12. Daku G and Vad J. Preliminary design guidelines for considering the vibration and noise of low-speed axial fans due to profile vortex shedding. *International Journal of Turbomachinery Propulsion and Power* 2022; 7. DOI: 10.3390/ijtpp7010002.
13. Reynolds SB, Gorrell SE and Estevadeordal J. Particle image velocimetry analysis on the effect of stator loading on transonic blade-row interactions. *Journal of Turbomachinery-Transactions of the Asme* 2012; 134. DOI: 10.1115/1.4006585.
14. Moghadam SMA, Loosen S, Meinke M, et al. Reduced-order analysis of the acoustic near field of a ducted axial fan. *International Journal of Heat and Fluid Flow* 2020; 85. DOI: 10.1016/j.ijheatfluidflow.2020.108657.
15. Gaetani P and Persico G. Influence of the rotor-driven perturbation on the stator-exit flow within a high-pressure gas turbine stage. *International Journal of Turbomachinery Propulsion and Power* 2021;

6. DOI: 10.3390/ijtpp6030028.

16. Huang X and Wang DX. Time-space spectral method for rotor-rotor/stator-stator interactions. *Journal of Turbomachinery-Transactions of the Asme* 2019; 141. DOI: 10.1115/1.4044771.
17. Gao J, Zheng Q, Li YJ, et al. Effect of axially non-uniform rotor tip clearance on aerodynamic performance of an unshrouded axial turbine. *Proceedings of the Institution of Mechanical Engineers Part a-Journal of Power and Energy* 2012; 226: 231-244. DOI: 10.1177/0957650911426671.
18. Taira K, Brunton SL, Dawson STM, et al. Modal analysis of fluid flows: an overview *AIAA Journal* 2020; 58: AU9-AU9. DOI: 10.2514/1.J056060.c1.
19. Taira K, Hemati MS, Brunton SL, et al. Modal analysis of fluid flows: applications and outlook. *AIAA Journal* 2020; 58: 998-1022. DOI: 10.2514/1.J058462.
20. Shim YM, Sharma RN and Richards PJ. Proper orthogonal decomposition analysis of the flow field in a plane jet. *Experimental Thermal and Fluid Science* 2013; 51: 37-55. DOI: 10.1016/j.expthermflusci.2013.06.014.
21. Zhao M, Zhao Y, Liu Z, et al. Proper orthogonal decomposition analysis of flow characteristics of an airfoil with leading edge protuberances. *Aiaa Journal* 2019; 57: 2710-2721. DOI: 10.2514/1.J058010.
22. Murray NE and Ukeiley LS. An application of Gappy POD - For

subsonic cavity flow PIV data. *Experiments in Fluids* 2007; 42: 79-91. DOI: 10.1007/s00348-006-0221-y.

23. Cizmas PGA and Palacios A. Proper orthogonal decomposition of turbine rotor-stator interaction. *Journal of Propulsion and Power* 2003; 19: 268-281. DOI: 10.2514/2.6108.
24. Sajadmanesh SM, Mojaddam M, Mohseni A, et al. Numerical identificaticin of separation bubble in.an ultra-high-lift turbine cascade using URANS simulation and proper orthogonal decomposition. *Aerospace Science and Technology* 2019; 93. DOI: 10.1016/j.ast.2019.105329.
25. Luo J. Design optimization of the last stage of a 4.5-stage compressor using a POD-based hybrid model. *Aerospace Science and Technology* 2018; 76: 303-314. DOI: 10.1016/j.ast.2018.01.043.
26. Anand Y, Verma SK, Anand S, et al. Transient 3-D modelling of ceiling fan for achieving thermal comfort. *Building Performance Analysis Conference and SimBuild*. Chicago, LA2018, p. 197-204.
27. Shi M-S, Chi P-A and Chen W-L. Prediction on turbomachinery flows using advanced turbulence models. *Journal of Aeronautics, Astronautics and Aviation* 2019; 51: 159-170. DOI: 10.6125/JoAAA.201906_51(2).02.
28. Yang J and Wu H. Explicit coupled solution of two-equation k- SST turbulence model and its application in turbomachinery flow simulation. *Hangkong Xuebao/Acta Aeronautica et Astronautica Sinica* 2014; 35: 116-124. DOI: 10.7527/S1000-6893.2013.0374.

29. Eckart C and Young G. The approximation of one matrix by another of lower rank. *Psychometrika* 1936; 1: 211-218.
30. Berkooz G, Holmes P and Lumley JL. The proper orthogonal decomposition in the analysis of turbulent flows. *Annual review of fluid mechanics* 1993; 25: 539-575.
31. Holmes P, Lumley JL, Berkooz G, et al. *Turbulence, coherent structures, dynamical systems and symmetry*. Cambridge university press, 2012.
32. Schlegel M, Noack BR, Jordan P, et al. On least-order flow representations for aerodynamics and aeroacoustics. *Journal of Fluid Mechanics* 2012; 697: 367-398. DOI: 10.1017/jfm.2012.70.
33. Lu H, Xiao Y, Liu Z, et al. Simulation and experimental research on aerodynamic noise of gas turbine 1.5-stage axial compressor. *Applied Acoustics* 2022; 192: 108722. DOI: https://doi.org/10.1016/j.apacoust.2022.108722.